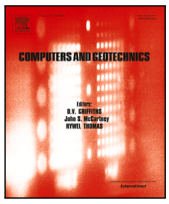
Computers and Geotechnics 203 (2027) 108706



Contents lists available at ScienceDirect

Computers and Geotechnics

journal homepage: www.elsevier.com/locate/compgeo



Research paper

Consistent dilatancy-based constitutive model of rock salt for geo-energy storage applications: An open-source numerical implementation

Ishmael D. Yevugah, Antoine B. Jacquey *

Polytechnique Montréal, Department of civil, geological and mining engineering, 2500, chemin de Polytechnique, Montréal, H3T 1J4, QC, Canada

ARTICLE INFO

Keywords:
Rock salt
Mechanical constitutive model
Dilatancy criterion
Geo-energy storage
Salt cavern design
Implicit integration scheme

ABSTRACT

Accurate numerical simulation of salt cavern performance in underground geo-energy storage of hydrogen, natural gas, compressed air, and CO_2 requires the integration of precise design criteria into a rigorous mechanical constitutive framework. This framework should be consistent with the design criteria, describing all mechanical loading (either short or long-term) deformations with a single parameter set. Due to methodological disconnects between the experimental derivation of design criteria and constitutive laws, only a limited number of consistent constitutive models exist in the literature. The RTL2020 model exemplifies such a mechanical constitutive law by incorporating dilatancy both as a feature in the mechanical constitutive model and as a design criterion, enabling accurate prediction of either short- or long-term mechanical deformations, including volumetric strain, with a single parameter set. This study presents a novel numerical implementation strategy for the RTL2020 model within an open-source simulator. The approach employs a stress–strain update algorithm using Newton–Raphson iterations with an adaptation of the classical implicit integration scheme (elastic predictor-inelastic corrector). This formulation ensures unconditional stability, rapid convergence, high numerical accuracy and low computational cost at the constitutive level. Validation against experimental data confirms the model's capacity to reproduce key mechanical behaviours of rock salt, including the negligible influence of mean pressure on axial and deviatoric strains and the strong sensitivity of volumetric strain to mean pressure. These results underscore the robustness of our implementation. Application of the model to numerical triaxial cyclic-loading simulations further reveals a profound dependence of deformation rate and mechanism on loading frequency and stress amplitude, which has important implications for the long-term performance of hydrogen storage caverns in rock-salt formations. The model is open-source, making it readily accessible to the geomechanics community as a reliable tool for salt cavern design in geo-energy storage.

1. Introduction

Salt cavern design for underground geo-energy storage involves simulating cavern performance with adequate mechanical constitutive law, and specifying accurate design criteria, to effectively assess the cavern's serviceability and stability risks (Khaledi et al., 2016; Labaune et al., 2018; Labaune and Rouabhi, 2019; Rouabhi et al., 2019). Various constitutive models have been developed to describe the complex mechanical behaviour of rock salt (e.g. Berest et al., 2008; Tijani, 2008; Munson and Dawson, 1981; Gunther et al., 2010; Günther et al., 2015; Aubertin et al., 1993; Cristescu et al., 1994; Heusermann et al., 2003; Hou, 2003; Wolters et al., 2012), while corresponding design criteria have been proposed to evaluate the salt cavern's stability. The design criteria involve specifying allowable limits of key mechanical quantities (stress, strain and strain-rate) that the material can safely withstand. These limits are generally derived from established thresholds of rock salt's tensile or compressive strength.

Design criteria can be classified as either stress-based or strain-based (Labaune et al., 2018; Labaune and Rouabhi, 2019). Within these classifications are the tensile and dilatancy criteria (Sobolik and Ehgartner, 2011; Yang et al., 2016; Moghadam et al., 2015; Shahmorad et al., 2016; Wang et al., 2016). The dilatancy criteria defines the rock salt's contracting and dilating behaviour and are often determined through short-term triaxial tests (Rouabhi et al., 2019; Labaune and Rouabhi, 2019). Strain-based dilatancy criteria have strong limitations due to their empirical nature, while stress-based dilatancy criteria have limitations regarding proper correlation with creep laws (Labaune et al., 2018).

Traditionally, the design criteria have been applied as a post-processing step immediately following cavern simulation (Wang et al., 2015; Minkley et al., 2016; Labaune et al., 2018). However, this approach poses significant challenges, as it overlooks the potential for damage to occur at levels that may be undetected, even while

* Corresponding author.
E-mail address: antoine.jacquey@polymtl.ca (A.B. Jacquey).

https://doi.org/10.1016/j.compgeo.2026.108706
Received 2 July 2026; Received in revised form 14 September 2026; Accepted 29 September 2026
Available online 7 October 2026
0266-352X/© 2026 The Authors. Published by Elsevier Ltd. This is an open access article under the CC BY license (http://creativecommons.org/licenses/by/4.0/).

the cavern continues to operate safely until the simulation concludes (Labaune and Rouabhi, 2019). In this case, it is reasonable to assume that the stress state, affected by dilatancy and tensile phenomena, deteriorates during the simulation. Therefore, assessing the stress state at the cavern wall long after the design criteria have been exceeded holds little practical relevance. Recent advancements have addressed this issue by directly integrating design criteria into mechanical constitutive models to keep track with failure directly during numerical simulations, allowing for a more comprehensive approach to salt cavern design.

Despite the advancements, challenges persist in ensuring that rock salt mechanical constitutive models and their corresponding design criteria are derived using a consistent methodology, especially for salt cavern design (Rouabhi et al., 2019; Labaune et al., 2018; Labaune and Rouabhi, 2019). The historical separation between design criteria and constitutive laws contributes to this issue. Most existing rock salt mechanical models (e.g. Munson and Dawson, 1981; Aubertin et al., 1993; Cristescu et al., 1994; Heusermann et al., 2003; Hou, 2003) are based on long-term creep laboratory experiments, whereas design criteria are typically derived from short-term triaxial experiments (Hunsche, 1993). This methodological mismatch creates a disconnect between the mechanical constitutive models and their design criteria because short-term (triaxial) tests involve significantly higher loading rates than long-term tests, resulting in different parameters and data inconsistencies (Labaune et al., 2018; Labaune and Rouabhi, 2019). Although integrating the disconnected models (i.e., the mechanical constitutive models and the corresponding design criteria) is feasible under consistent laboratory and field conditions, such as temperature, stress, pressure, and loading rates, discrepancies between experimental and field conditions can introduce margins of error in the design process (Labaune and Rouabhi, 2019).

The RTL model (Labaune et al., 2018; Labaune and Rouabhi, 2019; Rouabhi et al., 2019) addresses these challenges by employing a unified mechanical model that integrates dilatancy directly into rock salt mechanical constitutive framework, while using the onset of this dilatancy as the design criterion. This integration effectively resolves the methodological disconnect between constitutive laws and design criteria by providing a single cohesive law (Labaune et al., 2018; Labaune and Rouabhi, 2019). This cohesive law is able to describe both short and long-term (creep) deformations with a single parameter set (Blanco-Martín et al., 2023). Unlike existing strain-based models, the RTL model is unrestricted by empirical evidence. Furthermore, the strain-based approach of the RTL model shifts the focus of instability evaluation from failure surfaces (cavern walls) to the volume of cavern wall that fails, allowing for more accurate and precise analyses of cavern performance (Labaune and Rouabhi, 2019).

The RTL model is an extension of Lemaitre's model (Tijani, 2008), accounting for the dilatancy through the mean stress. The RTL model, however, has limitations in accurately predicting long-term (creep) deformations, therefore it was further enhanced into the RTL2020 model (Azabou et al., 2021) by incorporating a second deviatoric term inspired by the transient component of the Munson-Dawson model (Munson and Dawson, 1981). This new term includes characteristic time and saturation strain dependencies of the stress deviator. The RTL2020 model therefore ensures a more accurate long-term (creep) behaviour prediction, balancing between the Lemaitre model's overly optimistic creep predictions and the excessively cautious estimates of the Munson-Dawson model when simulating transient and steady-state creep of rock salt (Azabou et al., 2021).

In this study, we present a comprehensive and novel numerical formulation for the RTL2020 constitutive model and its implementation in an open-source numerical simulator. The formulation is founded on a strain-stress update procedure that adapts the classical implicit numerical integration, commonly referred to as the elastic predictor–inelastic corrector method (Simo and Hughes, 1998; Dunne and Petrinic, 2005). A central feature of the implementation is the iterative solution of the strain and stress invariants, which are integral to both the RTL2020 model formulation and the stress update procedure. These iterations are efficiently resolved using the Newton–Raphson method, thus ensuring numerical accuracy, while providing unconditional stability and improved numerical convergence at low computational cost.

The open-source implementation of the model ensures that it is readily accessible to the geomechanics community, offering a robust constitutive model for evaluating the mechanical behaviour of rock salt in the context of salt cavern design for geo-energy storage.

The remainder of this paper is organized as follows. Section 2 presents the detailed formulations of the RTL2020 model and the numerical implementation strategy. Section 3 reports numerical benchmark tests that validate key components of the RTL2020 model implementation against analytical solutions. Section 4 provides a full validation of the model using experimental data. Section 5 applies the implemented model to assess rock salt mechanical behaviour during prolonged cyclic loading under varied periodic cycles. Section 6 provides a summary and conclusion of the study.

2. RTL2020 model & numerical implementation strategy

This section provides a detailed description of the RTL2020 constitutive model, as first introduced by Azabou et al. (2021), and our approach to its numerical implementation into an open-source numerical simulator called BEAVER (Jacquey and Yevugah, 2026). BEAVER is a comprehensive simulator for multiphysics geomechanics. It includes a repository of constitutive laws for describing the mechanical behaviour of geomaterials, particularly in the context of geo-energy applications. The simulator is built upon the MOOSE framework (Harbour et al., 2025), an open-source, multiphysics finite element platform developed by the Idaho National Laboratory. MOOSE offers a flexible and scalable environment, supporting hybrid parallel computations for solving complex multicomponent and multiphysics problems using implicit solution techniques and automatic differentiation capability (Lindsay et al., 2021).

2.1. Constitutive framework/formulation

The RTL2020 model (Azabou et al., 2021), as previously noted, improves the RTL model (Labaune et al., 2018; Labaune and Rouabhi, 2019; Rouabhi et al., 2019) by incorporating a second deviatoric transient creep mechanism. This additional component enhances the model's ability to accurately predict long-term creep behaviour, addressing the limitations observed in Lemaitre (Tijani, 2008) and Munson-Dawson models (Munson and Dawson, 1979, 1981). Specifically, the RTL2020 model achieves balance by mitigating the overly optimistic long-term predictions characteristic of the Lemaitre model, while also avoiding the overly conservative estimates associated with the Munson-Dawson model when simulating both transient and steady-state creep of rock salt.

The formulations of the RTL and RTL2020 models are rooted in a stress tensor (σ_{ij}) decomposition into a deviatoric and spherical components as follows:

$$\sigma_{ij} = \sqrt{\frac{2}{3}}\, q\, J_{ij} - \sqrt{3}\, p\, I_{ij}, \tag{1}$$

where the mean stress p and the von Mises equivalent stress q are defined as follows:

$$p = -\frac{\sigma_{kk}}{3}, \quad q = \sqrt{\frac{3}{2}\tau_{ij} : \tau_{ij}}. \tag{2}$$

J_{ij} and I_{ij} represent orthonormal bases for the stress tensor, defined as follows:

$$J_{ij} = \frac{\tau_{ij}}{\|\tau_{ij}\|}, \quad I_{ij} = \frac{\delta_{ij}}{\sqrt{3}}, \tag{3}$$

where $\tau_{ij} = \sigma_{ij} + p\,\delta_{ij}$ is the deviatoric stress tensor. By analogy of the stress decomposition, the viscoplastic strain rate tensor is split into a deviatoric and a volumetric components, as follows:

$$\dot{\epsilon}^{vp}_{ij} = \left(\sqrt{\frac{3}{2}}\,\dot{\gamma}^{vp}\,J_{ij}\right) - \left(\frac{1}{\sqrt{3}}\,\dot{\zeta}^{vp}\,I_{ij}\right), \tag{4}$$

where the effective deviatoric viscoplastic strain rate ($\dot{\gamma}^{vp}$) and the volumetric viscoplastic strain rate ($\dot{\zeta}^{vp}$) are the strain rate invariants defined as follows:

$$\dot{\gamma}^{vp} = \sqrt{\frac{2}{3}\,\dot{e}^{vp}_{ij} : \dot{e}^{vp}_{ij}}, \quad \dot{\zeta}^{vp} = -\dot{\epsilon}^{vp}_{kk}, \tag{5}$$

where $\dot{e}^{vp}_{ij} = \dot{\epsilon}^{vp}_{ij} + \frac{1}{3}\dot{\zeta}^{vp}\,\delta_{ij}$ is the deviatoric viscoplastic strain rate tensor. Substituting Eq. (3) into Eq. (4) gives an expression of the viscoplastic strain rate tensor based on its invariants and those of the stress tensor:

$$\dot{\epsilon}^{vp}_{ij} = \left(\frac{3}{2}\,\dot{\gamma}^{vp}\,\frac{\tau_{ij}}{q}\right) - \left(\frac{1}{3}\,\dot{\zeta}^{vp}\,\delta_{ij}\right). \tag{6}$$

The notation $\dot{\gamma}^{vp}$ refers to the effective deviatoric viscoplastic strain rate, comprising the modified Lemaitre creep mechanism from the RTL model and a second creep mechanism introduced in the RTL2020 version (Azabou et al., 2021; Blanco-Martín et al., 2024):

$$\dot{\gamma}^{vp} = \dot{\gamma}_L + \dot{\gamma}_R, \tag{7}$$

where $\dot{\gamma}_L$ is the Lemaitre effective deviatoric viscoplastic strain rate. It evolves as follows (Blanco-Martín et al., 2024; Azabou et al., 2021):

$$\frac{\mathrm{d}\gamma_L^{1/\alpha}}{\mathrm{d}t} = \left(\frac{q}{K(T)}\right)^{n_2}, \tag{8}$$

where $n_2 = \beta/\alpha$ and $K(T) = A_2 \exp\left(A_L \frac{\alpha}{\beta}\left(1 - \frac{T}{T_r}\right)\right)$. α, β, A_2, and A_L are positive rheological constants and T_r is a reference temperature at which A_2 is determined. Note that $0 < \alpha < 1$ (Azabou et al., 2021; Blanco-Martín et al., 2024).

Expanding Eq. (8) and including the exponential function of the temperature gives (Azabou et al., 2021; Blanco-Martín et al., 2024):

$$\dot{\gamma}_L = \alpha \exp\left(A_L\left(\frac{1}{T_r} - \frac{1}{T}\right)\right)\left(\frac{q}{A_2}\right)^{n_2} \gamma_L^{1-\frac{1}{\alpha}}. \tag{9}$$

This equation confirms the transient nature of Lemaitre's model, as $\dot{\gamma}_L$ is not constant and tends to approach zero asymptotically while $\frac{\mathrm{d}\gamma_L^{1/\alpha}}{\mathrm{d}t}$ remains constant at constant stress and temperature (q and T) (Blanco-Martín et al., 2024).

The additional equivalent deviatoric viscoplastic rate term, $\dot{\gamma}_R$, is an extra transient term inspired by the proportionality function in the transient component of the Munson-Dawson model (Munson and Dawson, 1981) and includes a characteristic time and saturation strain dependencies of the stress deviator. The model ensures a more accurate long-term creep prediction, balancing between the Lemaitre model's overly optimistic long-term creep predictions and the excessively cautious estimates of the Munson-Dawson model when simulating transient and steady-state creep of rock salt (Azabou et al., 2021). It is a function of internal state variables (σ, T, γ_R) and is defined as follows:

$$\dot{\gamma}_R = \begin{cases} A\left(1 - \frac{\gamma_R}{\bar{\gamma}_R}\right)^n R(\sigma,T), & \text{if } \gamma_R \le \bar{\gamma}_R, \\ -B\left(\frac{\gamma_R}{\bar{\gamma}_R} - 1\right)^m R(\sigma,T), & \text{if } \gamma_R \ge \bar{\gamma}_R, \end{cases} \tag{10}$$

where A, B, m, and n are material parameters, with $A > 0$, $B > 0$, and $m > 1$, $n > 1$ (Azabou et al., 2021). The parameter $\bar{\gamma}_R$ describes the saturation strain, similar to that expressed in the Munson-Dawson model, and is defined as:

$$\bar{\gamma}_R(\sigma_{ij}) = \left\langle \frac{q}{A_1} \right\rangle^{n_1}, \tag{11}$$

where A_1 and n_1 are material parameters. The function R in Eq. (10) corresponds to the evolution of the hardening parameter in Lemaitre's model, ensuring that $\dot{\gamma}_L$ and $\dot{\gamma}_R$ have values of similar order of magnitude (Azabou et al., 2021):

$$R(\sigma,T) = \exp\left(A_R\left(\frac{1}{T_r} - \frac{1}{T}\right)\right)\left\langle \frac{q}{A_2} \right\rangle^{n_2}. \tag{12}$$

A notable advantage of formulating γ_R this way is that it is easy to integrate compared to the exponential formulation used in the Munson-Dawson transient model. Azabou et al. (2021) provides an analytical solution for the new viscoplastic distortion term, under constant stress and temperature.

In the RTL2020 model, the volumetric viscoplastic strain rate, $\dot{\zeta}^{vp}$, is defined as:

$$\dot{\zeta}^{vp} = z\,\frac{\langle p/N_z\rangle^{n_z} - \gamma^{vp}}{\langle p/M_z\rangle^{m_z} + \gamma^{vp}}\,\dot{\gamma}^{vp}, \tag{13}$$

where z, N_z, M_z, n_z, and m_z are material parameters (Azabou et al., 2021). From this definition of the volumetric viscoplastic strain rate, the dilatancy criterion is defined as:

$$\dot{\zeta}^{vp} < 0. \tag{14}$$

A notable feature of the RTL2020 model is its ability to account for reverse creep, based on the parameter B in Eq. (10). However, the drawback is that it includes more parameters than the Lemaitre or RTL models, which complicates the identification and accurate calibration of these parameters (Azabou et al., 2021).

2.2. Creep model and stress update algorithm

In the following, we present the procedure adopted to update the creep strain together with its implementation strategy. The primary variables for the update are the increments of the viscoplastic strain invariants. To determine the stress tensor, we employ a stress update procedure based on an implicit numerical integration scheme (Simo and Hughes, 1998; Dunne and Petrinic, 2005). This scheme follows a similar approach used in the open-source LEMUR numerical code (Jacquey et al., 2021).

The stress update procedure is formulated based on the total strain increment tensor rather than the total strain rate tensor to prevent the computed strain rate magnitude from varying with the choice of time-step size. This approach provides flexibility in selecting the time-step size without compromising accuracy, while also ensuring unconditional numerical stability. To advance the numerical simulation by a time increment in this stress update scheme, the current stress state at a given point is first updated using an increment of the total strain tensor, resulting in a trial stress noted σ^{tr}_{ij}. Then, in a second step, an inelastic strain increment tensor is calculated to correct the stress state to insure its compatibility with the creep laws. Hence, this scheme effectively combines elastic prediction with inelastic correction to maintain simulation accuracy. Thus, it is sometimes referred to as the elastic-predictor-inelastic-corrector scheme (Simo and Hughes, 1998; Dunne and Petrinic, 2005). This stress-update algorithm was originally used for plasticity models but has been adapted in this study for the RTL2020 viscoplasticity model.

The following elaborates on how the RTL2020 mathematical formulation is used for the implicit numerical integration scheme within the BEAVER numerical simulator. For all mathematical quantities, we use the superscript (k) to denote the current time-step. First, we compute the trial stress tensor as follows:

$$\sigma^{tr,(k)}_{ij} = \sigma^{(k-1)}_{ij} + \mathbb{C}_{ijkl} : \Delta\epsilon^{(k)}_{kl}, \tag{15}$$

where $\mathbb{C}_{ijkl}$ is the elasticity tensor, $\sigma^{(k-1)}_{ij}$ is the stress at the previous time step, and $\Delta\epsilon^{(k)}_{kl}$ is the total strain increment tensor.

Next, we compute the inelastic strain rate used to correct the trial stress tensor. This step is the core of the update procedure as it requires

an iterative approach. A general expression of the inelastic strain rate is as follows, with a dependency on the current stress tensor:

$$\dot{\varepsilon}_{ij}^{ie} = f\left(\sigma_{ij}\right). \tag{16}$$

Here, the function f is the inelastic deformation function which can be non-linear (either viscous, plastic or viscoplastic), and in this case, it is the RTL2020 viscoplastic model ($\dot{\varepsilon}_{ij}^{ie} = \dot{\varepsilon}_{ij}^{vp}$). Once the inelastic strain rate is obtained, the trial stress is corrected as follows:

$$\sigma_{ij}^{(k)} = \sigma_{ij}^{tr,(k)} - \mathbb{C}_{ijkl} : \Delta\varepsilon_{kl}^{vp,(k)}. \tag{17}$$

Eq. (6) can be used to reconstruct the viscoplastic strain rate tensor based on its invariants.

The challenge lies in implementing a routine to obtain the highly non-linear inelastic strain rate function shown in Eq. (16). For the RTL2020 model, this non-linearity occurs in the expressions for the strain rate invariants (i.e., $\dot{\gamma}_L$, $\dot{\gamma}_R$, and $\dot{\zeta}^{vp}$). We use an iterative solver to compute the stable values of these strain rate invariants for each time step, together with the corresponding von Mises equivalent stress q and mean stress p.

Considering the split of the stress tensor introduced in Eq. (1) and of the viscoplastic strain rate tensor introduced in Eq. (6), the stress correction in Eq. (17) can also be split using the definition of the stress invariants:

$$q^{(k)} = q^{(k),tr} - 3G\,\Delta\gamma^{vp}, \tag{18a}$$

$$p^{(k)} = p^{(k),tr} - K\,\Delta\zeta^{vp}, \tag{18b}$$

where $\Delta\gamma^{vp}$ and $\Delta\zeta^{vp}$ are the increments of viscoplastic equivalent deviatoric and volumetric strain respectively.

We adopted a Newton–Raphson iterative approach to solve for the increments of the non-linear strain invariants ($\Delta\gamma_L$, $\Delta\gamma_R$, and $\Delta\zeta^{vp}$). Once we achieve convergence, we update the inelastic strain increment tensor and the stress tensor based on Eq. (17). In this Newton–Raphson scheme, we initialize the increments of the viscoplastic strain invariants to zero. To prevent a singularity associated with this initialization for the evaluation of the modified Lemaitre strain rate (Eq. (9)) when $\gamma_L = 0$, we adopt a simplified version of this equation for the first iteration of the first time step:

$$\dot{\gamma}_L\left(\gamma_L = 0\right) = \alpha \exp\left(A_L\left(\frac{1}{T_r} - \frac{1}{T}\right)\right)\left(\frac{q}{A_2}\right)^{n_2}. \tag{19}$$

With this simplified expression, the singularity is resolved while insuring that the strain rate is proportional to the loading, instead of assigning a prescribed absolute value. After a single Newton–Raphson iteration, the Lemaitre viscoplastic strain becomes positive and the exact expression from Eq. (9) is used.

Due to the dependence of the volumetric strain rate on the equivalent deviatoric strain rate, as shown in Eq. (13), we employed a sequential coupling approach. In this approach, we separately solved for the viscoplastic equivalent deviatoric strain increment in a first step, and the viscoplastic volumetric strain increment in a second step. This sequential coupling strategy does not induce any numerical error as the RTL2020 model is sequentially coupled in its design and not fully coupled.

For the equivalent viscoplastic strain, we define the following residual functions:

$$R_L\left(\Delta\gamma_L^{(i)}, \Delta\gamma_R^{(i)}\right) = \dot{\gamma}_L\left(\Delta\gamma_L^{(i)}, \Delta\gamma_R^{(i)}\right)\Delta t - \Delta\gamma_L^{(i)}, \tag{20a}$$

$$R_R\left(\Delta\gamma_L^{(i)}, \Delta\gamma_R^{(i)}\right) = \dot{\gamma}_R\left(\Delta\gamma_L^{(i)}, \Delta\gamma_R^{(i)}\right)\Delta t - \Delta\gamma_R^{(i)}, \tag{20b}$$

where the functions $\dot{\gamma}_L\left(\Delta\gamma_L^{(i)}, \Delta\gamma_R^{(i)}\right)$ and $\dot{\gamma}_R\left(\Delta\gamma_R^{(i)}, \Delta\gamma_R^{(i)}\right)$ are defined by Eqs. (9) and (10). The subscript i denotes the iteration number in the Newton–Raphson loop.

Differentiating the residuals give the Jacobians and a system of equations for solving the effective deviatoric viscoplastic strain increments, as follows:

$$\underbrace{\begin{bmatrix} \frac{\partial R_L}{\partial \Delta\gamma_L} & \frac{\partial R_L}{\partial \Delta\gamma_R} \\ \frac{\partial R_R}{\partial \Delta\gamma_L} & \frac{\partial R_R}{\partial \Delta\gamma_R} \end{bmatrix}}_{\text{Jacobian matrix}} \underbrace{\begin{bmatrix} \delta\Delta\gamma_L \\ \delta\Delta\gamma_R \end{bmatrix}}_{\text{increment vector}} = \underbrace{\begin{bmatrix} -R_L \\ -R_R \end{bmatrix}}_{\text{residual vector}} \tag{21}$$

or equivalently,

$$\begin{aligned} R_L + \frac{\partial R_L}{\partial \Delta\gamma_L}\,\delta\Delta\gamma_L + \frac{\partial R_L}{\partial \Delta\gamma_R}\,\delta\Delta\gamma_R = 0, \\ R_R + \frac{\partial R_R}{\partial \Delta\gamma_L}\,\delta\Delta\gamma_L + \frac{\partial R_R}{\partial \Delta\gamma_R}\,\delta\Delta\gamma_R = 0. \end{aligned} \tag{22}$$

The equivalent strain increments used in Eq. (20) are updated at each iteration with the increment vector, as follows:

$$\begin{aligned} \Delta\gamma_L^{(i+1)} = \Delta\gamma_L^{(i)} + \delta\Delta\gamma_L, \\ \Delta\gamma_R^{(i+1)} = \Delta\gamma_R^{(i)} + \delta\Delta\gamma_R. \end{aligned} \tag{23}$$

This system of residual equations are solved iteratively until the residual tolerances are satisfied and convergence is achieved, yielding the equivalent deviatoric viscoplastic strain increments ($\Delta\gamma_L$, $\Delta\gamma_R$).

Similarly, for the volumetric strain, the residual is as follows:

$$R_V = \dot{\zeta}^{vp}\left(\Delta\zeta^{vp,(i)}\right)\Delta t - \Delta\zeta^{vp,(i)} = 0, \tag{24}$$

where the function $\dot{\zeta}^{vp}\left(\Delta\zeta^{vp,(i)}\right)$ is given by Eq. (13).

Differentiating the residual gives the equation for solving the volumetric strain increment, as follows:

$$R_V + \frac{\partial R_V}{\partial \Delta\zeta^{vp}}\,\delta\Delta\zeta^{vp} = 0. \tag{25}$$

This residual equation is solved iteratively until the residual tolerance is satisfied and convergence is achieved, yielding the volumetric strain increment ($\Delta\zeta_{vp}$). The obtained quantities of viscoplastic strain increments are then injected into Eq. (18) to update the stress invariants.

The novelty of our stress update algorithm lies in the iterative approach adopted for solving and updating the stress invariants q and p at each time step, which are essential for computing the strain rate invariants. Unlike existing implementations of the RTL (Blanco-Martín et al., 2024) and RTL2020 (Azabou et al., 2021) models that use direct update procedure without iterating these values at each time step, our method ensures more accurate solutions, enabling unconditional stability in the numerical simulation without limiting the choice of time step size (Hughes and Taylor, 1978). A direct comparison of the implicit update algorithm with an explicit update algorithm is summarized in Appendix. Note that despite the unconditional stability of the scheme, for highly-nonlinear viscoplastic models such as the RTL2020 model, convergence may prove difficult in the global solve. Fig. 1 summarizes how the stress update procedure is implemented in the BEAVER numerical simulator.

3. Numerical benchmark tests

We verified the accuracy of our RTL2020 model implementation by conducting numerical benchmark tests, focusing on the deviatoric strain rate component of the viscoplastic strain rate tensor. Particularly, we compared each implemented equivalent deviatoric strain rates (i.e., $\dot{\gamma}_L$ and $\dot{\gamma}_R$) to their respective analytical solutions to validate the accuracy of their implementation in the simulator.

3.1. Lemaitre's equivalent deviatoric viscoplastic strain rate

Considering only $\dot{\gamma}_L$ from Eq. (7), the deviatoric viscoplastic strain rate of the RTL2020 model becomes the Lemaitre model. The Lemaitre

Result: $\Delta\gamma_L$, $\Delta\gamma_R$, $\Delta\zeta^{vp}$

Initialization:

$\Delta\gamma_L^{(0)} = 0$, $\Delta\gamma_R^{(0)} = 0$, $\Delta\zeta^{vp,(0)} = 0$;

Effective deviatoric strain update:

$R_L^{(0)} = R_L(0,0)$, $R_R^{(0)} = R_R(0,0)$, $i = 0$;

while $\sqrt{(R_L^{(i)})^2 + (R_R^{(i)})^2} > tol$ **do**

Compute $\delta\Delta\gamma_L^{(i+1)}$, $\delta\Delta\gamma_R^{(i+1)}$ using Eq. 22;

Update deviatoric strain increments:

$\Delta\gamma_L^{(i+1)} = \Delta\gamma_L^{(i)} + \delta\Delta\gamma_L^{(i+1)}$;

$\Delta\gamma_R^{(i+1)} = \Delta\gamma_R^{(i)} + \delta\Delta\gamma_R^{(i+1)}$;

Update residuals:

$R_L^{(i+1)} = R_L\left(\Delta\gamma_L^{(i+1)}, \Delta\gamma_R^{(i+1)}\right)$;

$R_R^{(i+1)} = R_R\left(\Delta\gamma_L^{(i+1)}, \Delta\gamma_R^{(i+1)}\right)$;

Update iteration counter:

$i = i + 1$;

if $i > i_{max}$ **then**

Failed solve;

end

end

$\Delta\gamma^{vp} = \Delta\gamma_L + \Delta\gamma_R$;

Volumetric strain update:

$R_V^{(0)} = R_V(0)$, $i = 0$;

while $\left|R_V^{(i)}\right| > tol$ **do**

Compute $\delta\Delta\zeta^{vp,(i+1)}$ using Eq. 25;

Update volumetric strain increment:

$\Delta\zeta^{vp,(i+1)} = \Delta\zeta^{vp,(i)} + \delta\Delta\zeta^{vp,(i+1)}$;

Update residual:

$R_V^{(i+1)} = R_V\left(\Delta\zeta^{vp,(i+1)}\right)$;

Update iteration counter:

$i = i + 1$;

if $i > i_{max}$ **then**

Failed solve;

end

end

Update stress tensor:

$\sigma_{ij} = \sigma_{ij}^{tr} - 3G\,\Delta\gamma^{vp}\,\frac{\tau_{ij}^{tr}}{q^{tr}} + K\,\Delta\zeta^{vp}\,\delta_{ij}$;

Fig. 1. Stress update for RTL2020 model.

model assumes a purely transient flow for rock salt, with the viscoplastic strain rate decreasing asymptotically to zero (Azabou et al., 2021).

The Lemaitre equivalent viscoplastic strain rate ($\dot{\gamma}_L$) is outlined in Eq. (9). The integral of this equation gives the analytical solution, as shown below Boidy et al. (2002):

$$\gamma_L = \left(\frac{A}{\alpha}\right)^{\alpha}\left(\frac{q}{A_2}\right)^{\beta} t^{a}, \tag{26}$$

where A is a time-scaling model parameter unique to the material under consideration. Azabou et al. (2021) expressed this parameter in terms of the Arrhenius law in the RTL2020 model, where $A = \alpha \exp\left[A_L\left(\frac{1}{T_r} - \frac{1}{T}\right)\right]$, to describe the behaviour of rock salt. For isothermal conditions, we have $A = \alpha$.

To evaluate the accuracy of our numerical implementation, we conduct a three-dimensional (3D) uniaxial creep test simulation, illustrating a fundamental viscoplastic problem. The numerical results are compared to the analytical solution for validation. The test involves a cylindrical rock salt specimen subjected to a constant external uniaxial compressive stress (of 2 MPa) at a uniform and constant temperature. The uniaxial compressive stress (σ_a) is applied vertically at the top surface and maintained throughout the simulation (see Fig. 2). The specimen is constrained with fixed vertical displacement boundary conditions on the bottom surface, and the simulation is run for a duration of one day. The sample has a Young's modulus (E) and Poisson's ratio (ν) of 1000 MPa and 0.2 respectively. Table 1 shows the various parameters used for the modified Lemaitre model.

Table 1
Material properties for $\dot{\gamma}_L$ and $\dot{\gamma}_R$ numerical benchmarks.

Parameter	Value	Units
E	1000	MPa
ν	0.2	–
Modified Lemaitre ($\dot{\gamma}_L$)		
α	0.1	–
β	1.48	–
A_2	1	MPa d
Munson-Dawson ($\dot{\gamma}_R$)		
A	0.5	–
B	0.05	–
n	5	–
m	5	–
A_1	0.3	MPa m μm^{-1}
n_1	3	–
A_2	0.5	MPa d m μm^{-1}
n_2	4	–

As illustrated in Fig. 3, the model predicts uniaxial deformation consistent with the Lemaitre equivalent deviatoric viscoplastic strain rate. The numerical results closely match the analytical solution, validating our numerical implementation of $\dot{\gamma}_L$ within the RTL2020 model.

3.2. Modified Munson-Dawson's equivalent deviatoric viscoplastic strain rate

The second transient term ($\dot{\gamma}_R$) in Eq. (7), formulated based on the proportionality function of the transient Munson-Dawson model, admits an analytical solution, as follows (Azabou et al., 2021):

$$\gamma_R(t) = \gamma_{R0} + (\bar{\gamma}_R + \gamma_{R0})\,\xi(t), \tag{27}$$

where ξ is defined as:

$$\xi(t) = 1 - \left(\frac{1}{1 + V\left(t - t_0\right)}\right)^{\frac{1}{k-1}}, \tag{28}$$

and

$$V = (k-1)\,U\,\frac{A_1^{n_1}}{A_2^{n_2}}\,q^{n_2 - n_1}, \tag{29}$$

with:

$$\begin{cases} k = n; \quad U = A\left(1 - \frac{\gamma_{R0}}{\bar{\gamma}_R}\right)^{n-1}, \text{ when } \gamma_R \le \bar{\gamma}_R, \\ k = m; \quad U = B\left(\frac{\gamma_{R0}}{\bar{\gamma}_R} - 1\right)^{m-1}, \text{ when } \gamma_R \ge \bar{\gamma}_R. \end{cases} \tag{30}$$

To validate the accuracy of our numerical implementation of $\dot{\gamma}_R$, we considered a three-dimensional (3D) uniaxial creep test problem, analogous to the one described in Section 3.1 for $\dot{\gamma}_L$ (see Fig. 2). Instead of applying a constant uniaxial compressive stress on the top boundary of the finite element domain (i.e., the rock salt medium), we imposed a uniaxial compressive stress function: a constant 10 MPa uniaxial stress is maintained for 15 days, followed by a reduction to 5 MPa for another 15 days. The parameters used in this benchmark test are listed in Table 1.

As illustrated in the γ_R evolution plot in Fig. 4, the numerical model accurately captures the equivalent deviatoric viscoplastic strain

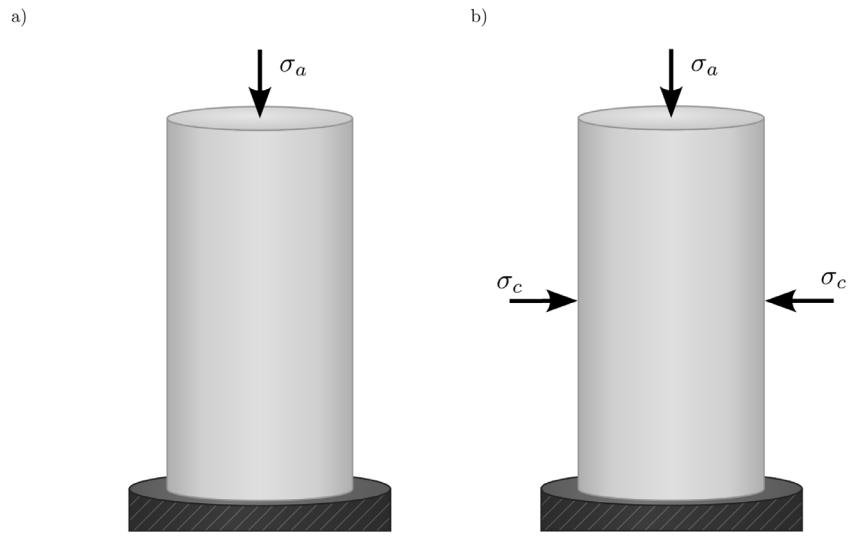


Fig. 2. Setup for the uniaxial compressive creep test used in both benchmark tests.

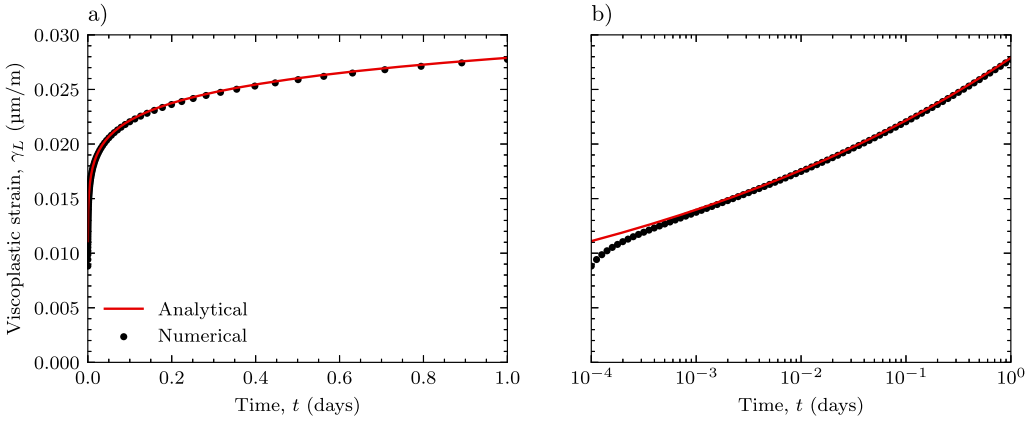


Fig. 3. Evolution of the scalar equivalent viscoplastic Lemaitre strain (γ_L) as a function of time. The analytical solution is given by Eq. (26).

deformation consistent with the analytical solution. This consistency validates our numerical implementation of the $\dot{\gamma}_R$ in the RTL2020 model.

4. Validation of the RTL2020 model against experimental data

The accuracy of the full RTL2020 model implementation was evaluated by validating it against experimental data from Mines ParisTech. Following the laboratory short-term (triaxial) and long-term (creep) experiments conducted by Blanco-Martín et al. (2023), we performed comprehensive validation simulations under complex loading paths to demonstrate the model's fit for both the triaxial and creep tests using a single parameter set, as reported in Blanco-Martín et al. (2023).

The short-term (triaxial) test considered in this validation is a strain-controlled test, where the lateral (confining) pressure (σ_c) is kept constant while imposing a specified axial strain rate. Two separate sets of tests are considered, performed at two different axial strain rates. For each set of tests (i.e. for a given axial strain rate), three different confining pressures are considered to assess the impacts of the mean stress on the volumetric response. The first set of triaxial tests was conducted under a constant axial strain rate of $\dot{\varepsilon}_a = 1.0 \times 10^{-6}\,\mathrm{s}^{-1}$ while the second test was performed at a higher constant strain rate of $\dot{\varepsilon}_a = 1.0 \times 10^{-5}\,\mathrm{s}^{-1}$ (as shown in Fig. 5).

The long-term (creep) test validation further corroborates the impact of mean pressure on the various strains of the rock salt. It involved a multi-stage creep test, with successive loading stages (i.e., applied axial stress) and differential stress levels. Three tests were considered for this validation, two of which were performed at an ambient temperature, while the last test was conducted at an elevated temperature. The first ambient temperature creep test was conducted at a constant confining pressure with multi-stage levels of axial stress and lasted for 75 days, while the second ambient temperature test was performed at varying confining pressure and axial stress while maintaining a constant mean pressure, spanning 300 days. The elevated temperature test was also carried out at a varying confining pressure but lasted for 200 days.

Table 2 provides a detailed list of all the parameters used to accurately fit the RTL2020 model to both the short-term (triaxial) and long-term (creep) experimental data (Blanco-Martín et al., 2023). The RTL2020 model calibration procedure has been comprehensively documented by Azabou et al. (2021).

Figs. 5 and 6 illustrate the results for the validation tests. The short-term (triaxial) test results (Fig. 5) show plots of differential stress versus the volumetric and the differential strains for the first and second short-term triaxial tests, respectively. As shown for each of these triaxial tests, the differential strain evolution for the three test variations are extremely close and almost aligned, consistent with the experimental observations. The volumetric strain responses, although in general agreement with the experimental data, are not perfect matches.

The multi-stage creep tests shown in Fig. 6 highlight the axial strain evolution at each loading stage for the three creep tests. This figure also shows the applied axial stress and lateral pressure for each creep

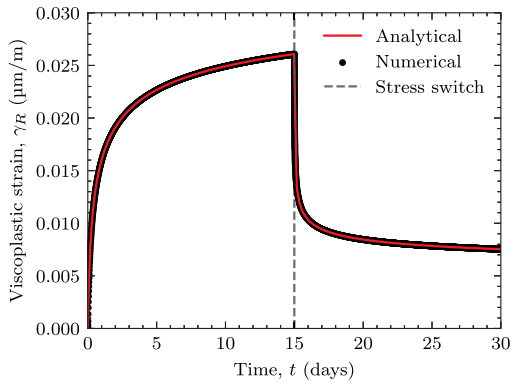


Fig. 4. Evolution of the scalar equivalent viscoplastic Munson-Dawson strain (γ_R) as a function of time. The analytical solution is given by Eq. (27).

Table 2
Parameters for short-term (axial loading), long-term (creep) and cyclic triaxial tests. Strain are in $\mu m\,m^{-1}$, stresses in MPa, time in days.

Parameter	Value	Units
E	22 360	MPa
ν	0.29	–
A_R	7870	–
Distortion ($\dot{\gamma}_L$ and $\dot{\gamma}_R$)		
α	0.5	–
A_1	0.148	$MPa\,m\,\mu m^{-1}$
n_1	2.04	–
A_2	2.63	$MPa\,d\,m\,\mu m^{-1}$
n_2	7.06	–
A	10	–
n	20.95	–
B	0.5	–
m	1.46	–
Dilatancy ($\dot{\zeta}^{vp}$)		
z	0.61	–
n_z	1.12	–
N_z	0.009	$MPa\,m\,\mu m^{-1}$
m_z	2.67	–
M_z	0.79	$MPa\,m\,\mu m^{-1}$

test. As observed, the axial strain evolves rather slowly, reaching only 2 % after 75 days of loading for the first ambient temperature creep test and approximately 3.5 % after 300 days for the second ambient temperature creep test. For the elevated temperature creep test, the axial strain reaches nearly 6 % after 200 days of loading.

The implemented RTL2020 model show strong capability in simulating rock salt behaviour under a range of complex loading conditions, including variations in loading rate and mean pressure. For example, the long term (creep) validation results show that changes in mean pressure at constant temperature has no significant influence on the evolution of equivalent strain, as evidenced by the similar slow strain evolution observed in both ambient temperature tests. This observation is consistent with the experimental findings reported by Blanco-Martín et al. (2023). We, however, note that despite the slow evolution of axial strain at elevated temperature, it is still relatively faster than the evolution rate at ambient temperature, indicating that temperature might play a significant role in strain evolution.

The negligible influence of the mean pressure on equivalent strain is further supported by the triaxial validation tests, as shown by the closeness of the deviatoric strain curves obtained for the different triaxial tests conducted at constant confining pressure. In contrast, volumetric strain exhibits clear sensitivity to mean pressure, as reflected in the increasing separation of volumetric strain curves across the three triaxial test variations. This effect is particularly evident in the observed dilatancy thresholds, where higher mean pressure requires greater deviatoric stress and longer loading duration to initiate dilation. This trend is also consistent with the experimental observations reported by Blanco-Martín et al. (2023), further confirming the reliability and accuracy of the RTL2020 model implementation.

5. Evaluation of rock salt mechanical behaviour during prolonged cyclic loading under varied periodic cycles

Transitioning to a low-carbon energy systems demands large-scale, flexible storage solutions capable of smoothing the disparity between renewable energy supply and consumption (Ramesh Kumar et al., 2023; Muhammed et al., 2023). Subsurface storage of energy carriers, such as CO_2, compressed air, and hydrogen, inside underground engineered salt caverns has emerged as a leading strategy in this context (Gholami, 2023; Tackie-Otoo and Haq, 2024). Rock salt formations are particularly advantageous due to their creep properties, ultra-low permeability and inherent self-healing mechanisms (Carter and Hansen, 1983; Senseny et al., 1992; Cristescu and Hunsche, 1998; Lüdeling et al., 2022), which together ensure long-term cavern integrity. Among the various energy carriers, hydrogen stands out because of its high energy density, enabling efficient storage within comparatively small cavern volumes (Böttcher et al., 2017; Tackie-Otoo and Haq, 2024).

However, the mechanical behaviour of rock salt under cyclic loading conditions relevant to subsurface hydrogen storage remains poorly understood. Underground hydrogen storage operations subject salt caverns to repeated internal pressure fluctuations associated with injection and withdrawal cycles (Wang et al., 2021; Liu et al., 2025). Each cycle increases and decreases the cavern pressure, imposing a corresponding cyclic mechanical load on the surrounding salt formation. These pressure variations are governed primarily by two operational parameters (Li et al., 2024; Bagchi et al., 2025; Dong et al., 2025): the loading amplitude, defined by the upper and lower operating pressure limits, and the cycle frequency or period, which reflects the rates of hydrogen injection and extraction. Both parameters strongly influence cavern stability, controlling the stress range and loading rate experienced by the cavern wall. Consequently, they affect the likelihood of onset of dilation.

We evaluate long-term cyclic loading of rock salt in the context of underground hydrogen storage using the RTL2020 constitutive model to characterize the associated mechanical response. Existing studies on this topic are predominantly experimental, with most focusing on short-term cyclic loading at relatively high frequencies (i.e., seconds and hourly periodic cycles) (Fan et al., 2019; Han et al., 2020; Wang et al., 2021; Zhao et al., 2022; Dong et al., 2025). Our study is particularly significant because hydrogen storage, unlike Compressed Air Energy Storage (CAES) systems and other green energy carriers, involves pressure cycles spanning several months to a year (Chang and Ross, 2025), usually with large periodic cycles. The capacity of the RTL2020 model to capture volumetric strain accumulation under such loading conditions additionally provides a distinct contribution, offering insights largely absent from existing literature.

To reproduce the mechanical effects of internal pressure cycling on a salt-cavern wall, a triaxial cyclic-compression simulation was performed under constant and uniform temperature conditions. The cylindrical rock-salt specimen is fixed at its bottom surface with a zero-displacement boundary condition, while a confining pressure (σ_c) of 4.5 MPa is applied uniformly around the outer boundary. Axial loading is imposed on the top surface in the form of stress cycles that varies between a maximum compressive load (σ_{max}) and a minimum load equal to the confining pressure (i.e., $\sigma_{min} = \sigma_c = 4.5$ MPa), ensuring a differential load note $\Delta\sigma_{load}$. This configuration ensures that the rock salt sample remains in compression throughout the unloading phase, and prevents tensile elongation.

Different loading scenarios are examined varying the cyclic period Δt_{load} (1, 2, 4, and 8 days) and the cyclic stress amplitude $\Delta\sigma_{load}$ (12.5, 13.5, 14.5, and 15.5 MPa). Each cycle consists of a linear loading

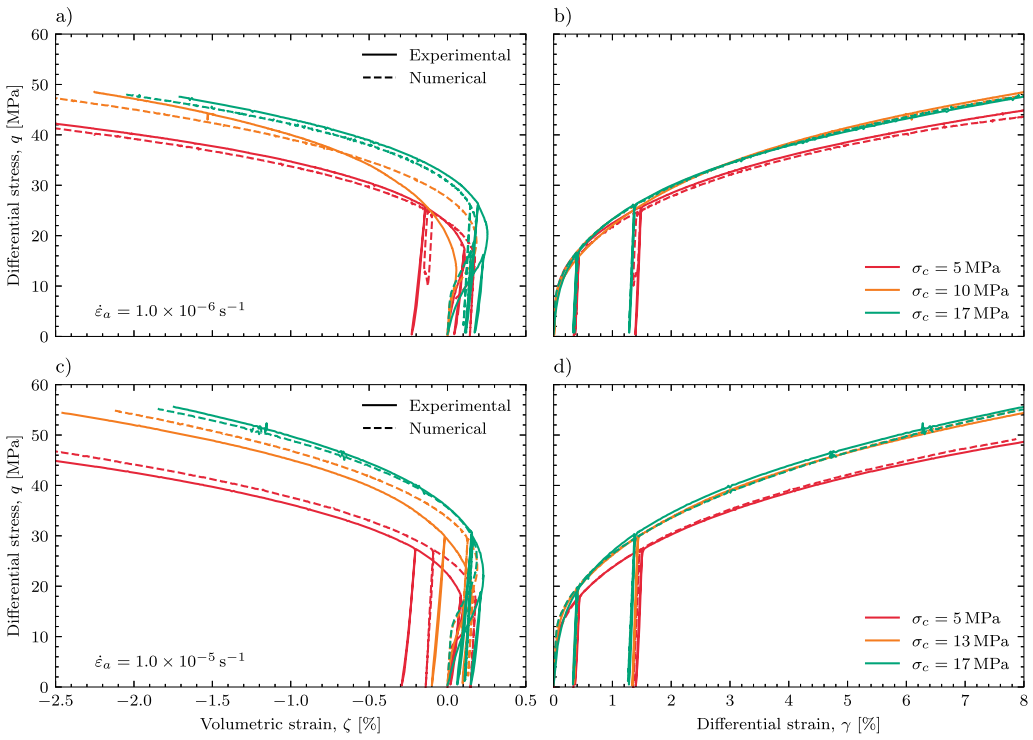


Fig. 5. Comparison of the RTL2020 model to short-term laboratory triaxial experiments. Top panels (a and b) show triaxial experiments performed at an axial strain rate of $1.0 \times 10^{-6}\,\mathrm{s}^{-1}$ and bottom panels (c and d) at an axial strain rate of $1.0 \times 10^{-5}\,\mathrm{s}^{-1}$.

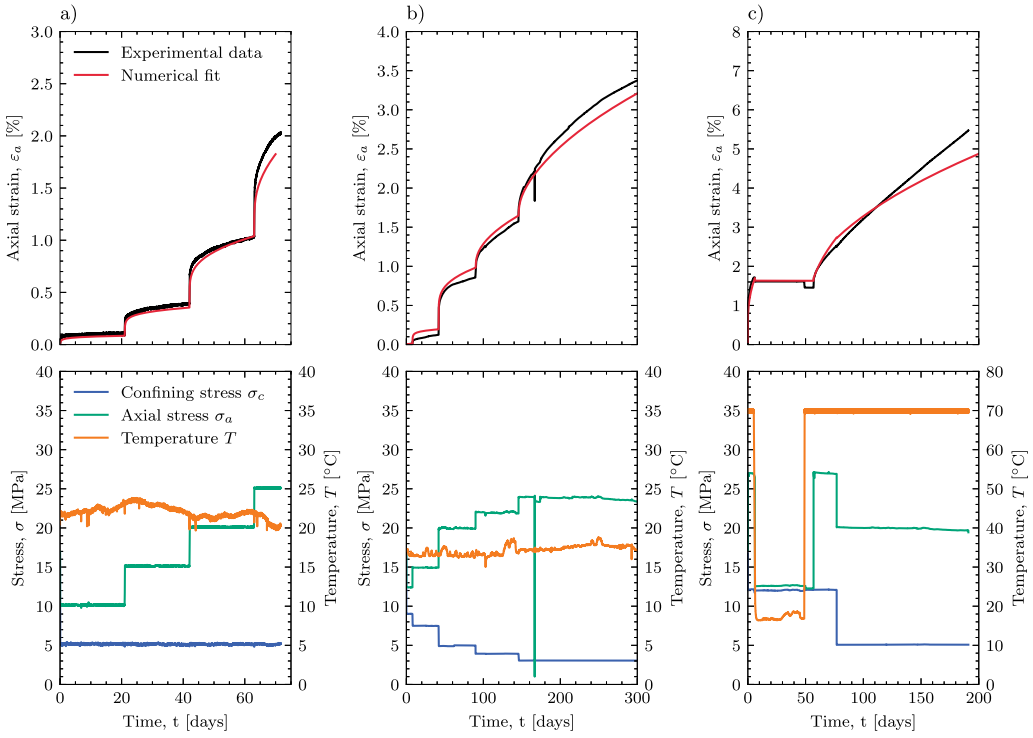


Fig. 6. Comparison of the RTL2020 model to long-term laboratory creep tests. Left panels (a) show a classic multistage creep test with different levels of differential stress. Middle panels (b) show a multistage creep test performed at constant mean stress. Right panels (c) show a multistage creep test with a drop of temperature.

phase, followed by an unloading phase as illustrated for 4 cycles in Fig. 7. The simulation runs for a total duration of 365 days (i.e., 12 months), allowing for the observation of long-term deformation trends and potential viscoplastic dilatancy. The salt sample is assigned the elastic and viscoplastic properties reported by Blanco-Martín et al. (2023), as provided in Table 2.

We interpreted the mechanical response of the rock salt through the evolution of axial strain, volumetric strain, and the stress–strain

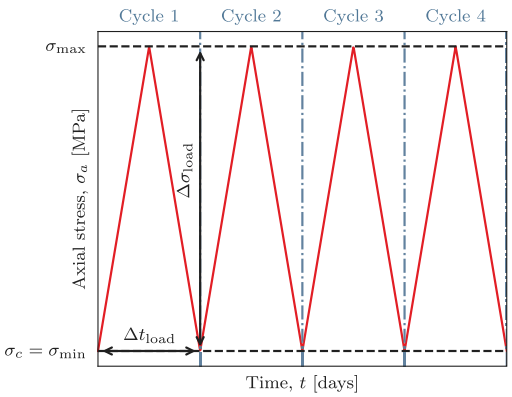


Fig. 7. Applied cyclic loading for four periodic loading/unloading cycles with loading period Δt_{load} and loading stress amplitude $\Delta\sigma_{load}$.

relation. These parameters are central to assessing long-term cavern stability and serviceability because they reveal the deformation rate and mechanism of the salt cavern wall under repeated pressure cycling.

The left panels of Fig. 8 show the evolution of the axial and volumetric strain over time for four different periods, Δt_{load} = 1, 2, 4 and 8 days and a constant stress amplitude $\Delta\sigma_{load}$ of 14.5 MPa. During the first 150 days, the axial strain response is relatively homogeneous among the four cycling periods, with an averaged response (not accounting for the rapid changes due to cyclic loading) close to a classic creep test. The axial strain rate is initially relatively high and gradually decreases over time until reaching a quasi-linear evolution of the axial strain, similar to a primary to secondary creep transition. After 150 days of cyclic loading, the axial strain evolution diverges. For all cyclic loading periods, the axial strain accelerates after the 150-day timestamp and gradually decreases, until reaching a quasi-linear evolution with time. The increase in axial strain rate is more pronounced for high frequency cyclic load (low cyclic loading period) than for low frequency cyclic load (high cyclic loading period). At the end of the simulated time, the absolute axial strain spans a significant value range depending on the cyclic loading period. The axial strain reaches values at around 2 % for the 1-day cyclic loading period and values around 1.25 % for the 8-day cyclic loading period.

During the first 150 days, the volumetric strain evolution reveals a complex pattern. During the first loading cycle, the sample exhibits an elastic compression. Then, the rock salt samples exhibit a short-lived dilation phase quickly followed by a re-compaction phase from day 20 to day 150 for all the cyclic loading periods considered. At the 150-day timestamp, the volumetric response changes with the onset of dilation. The volumetric strain starts increasing sharply at a decreasing rate over time, similar to what is observed for the axial strain evolution. The dilation is more pronounced for low frequency cyclic loading than for high frequency cyclic loading. After 365 days of simulated time, the volumetric strain reaches around +0.07 % for the 1-day cyclic loading period and −0.05 % for the 8-day cyclic loading period.

The right panels of Fig. 8 show the evolution of the axial and volumetric strain over time for four different stress amplitudes, $\Delta\sigma_{load}$ = 12.5, 13.5, 14.5 and 15.5 MPa at a constant period Δt_{load} = 2 days. The axial and volumetric strain responses exhibit a similar response to the left panels. The timing of the onset of the divergent behaviour (accelerating axial strain and dilatation) is however impacted by the cyclic loading amplitude $\Delta\sigma_{load}$. The highest the loading stress amplitude is, the earliest this shift in overall response occurs in time. For the lowest stress amplitude considered ($\Delta\sigma_{load}$ = 12.5 MPa), the response remains in a secondary creep regime with compression, and we did not observe accelerating axial strain nor dilation. The evolution of axial strain and volumetric strain for the other three cases are similar after the divergent behaviour, exhibiting a similar accelerating axial strain and a similar volumetric response.

Fig. 9 shows the axial stress–axial strain relation for two of the numerical experiments conducted with cyclic loading periods of Δt_{load} = 2 days and 8 days for a loading stress amplitude of $\Delta\sigma_{load}$ = 14.5 MPa. Stress–strain curves for viscoplastic geomaterials undergoing cyclic loading exhibit characteristic sparse and dense regions that predict the primary (transient), secondary (steady-state) and tertiary (accelerated) creep phases of the material (Guo et al., 2012; Wang et al., 2021; Dong et al., 2025). Sparse regions correspond to rapid, but large strain accumulation, indicating the occurrence of either primary or tertiary creep based on the intensity. Dense regions indicate slower, more gradual strain accumulation, a characteristic of steady-state creep. For both the 2-day and 8-day cyclic loading periods, a similar response is observed. During the first loading phase, a large axial stress is reached followed by a 3-period sparse region corresponding to the primary creep phase observed on the strain evolution plot. Then, a large dense region is observed for many cycles corresponding to the secondary creep hase on the strain evolution plot. After the 150-day timestamp marking the onset of dilation, a sparse region is observed corresponding to accelerating creep which attenuates into a low intensity sparse region and associated with the transition back to the secondary creep observed on the strain evolution plots. All the cyclic loading periods exhibit the same behaviour in the axial stress–axial strain relationship, the difference being that the higher the period is the sparser the plots are.

These results highlight the strong influence of cyclic loading frequency (or equivalently, the loading period) on the accumulated strain and dilatancy of rock salt. In particular, our results indicate a direct relationship between loading frequency and strain accumulation: the higher the applied frequency, the higher the resulting accumulated strain. The influence of the loading frequencies becomes only relevant after the onset of dilation, which occurred for all cyclic loading periods at the 150-day timestamp. This indicates that the time for the onset of dilation is independent of the loading frequency. The onset of dilation and accelerated viscoplastic strain is however strongly dependent on the loading stress amplitude.

6. Discussion

This study introduces a comprehensive implementation of the RTL2020 viscoplastic model, entailing a volumetric viscoplastic component. The implementation uses an implicit scheme relying on the elastic predictor–plastic corrector method which is unconditionally stable and avoid time step size restrictions as encountered in explicit schemes. We validated our implementation with analytical benchmarks and comparisons to a comprehensive experimental dataset. We finally performed numerical experiments to simulate cyclic loading of a rock salt sample, as more realistic conditions in the context of seasonal hydrogen storage. In the following, we provide key discussion points about our results and their implications for the design of salt cavern for hydrogen storage.

6.1. Advantages and drawbacks of the implicit stress update method

The main innovative aspect of the methodological approach adopted in this study is to use an implicit integration scheme for the RTL2020 model. Previous studies made use of explicit integration schemes to model rock salt behaviour with the RTL2020 model (Rouabhi et al., 2019; Labaune et al., 2018; Labaune and Rouabhi, 2019). Explicit integration schemes consist in a straightforward update of the viscoplastic strain rates based on the previous step stress tensor. The main advantage of explicit integration schemes of viscoplastic models are their simplicity and easy implementation. However, as the viscoplastic

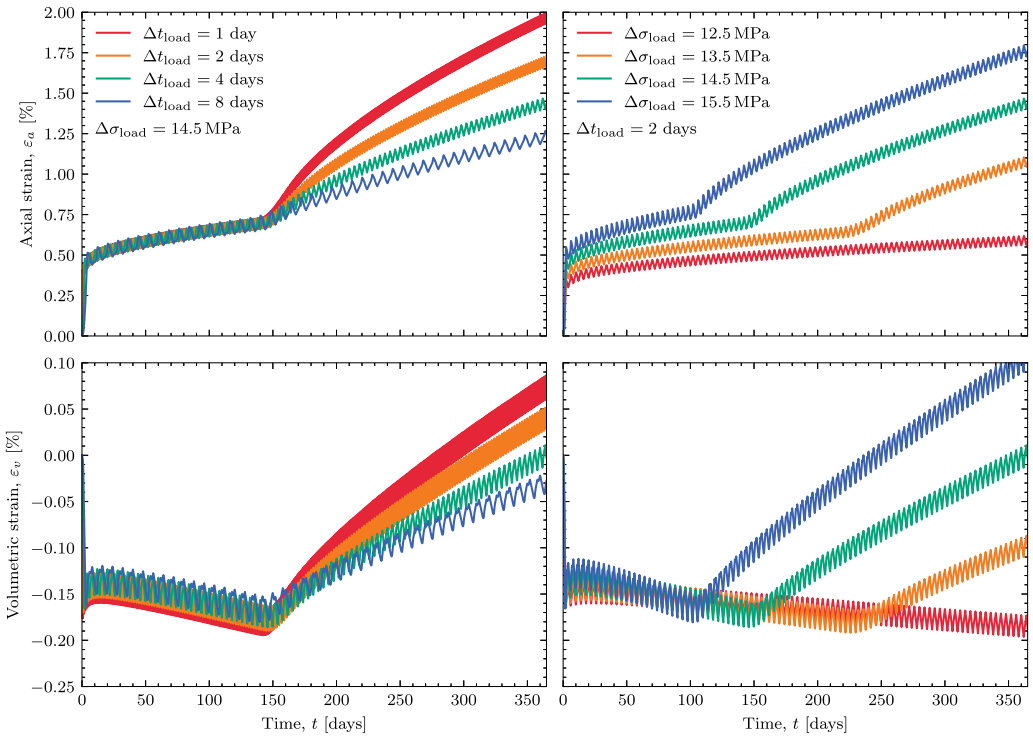


Fig. 8. Evolutions of the axial (top panels) and volumetric (bottom panels) strain with varying loading period Δt_{load} (left panels) and varying loading stress amplitude $\Delta\sigma_{\text{load}}$ (right panels).

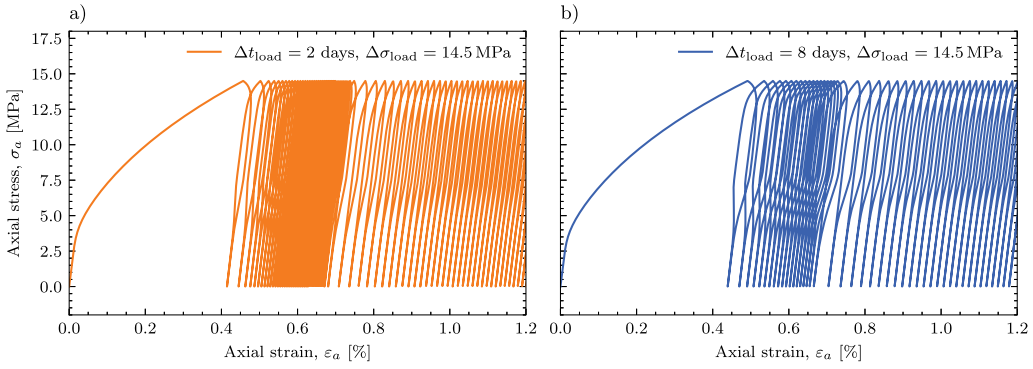


Fig. 9. Stress–strain curves for the 2 and 8-day periodic cycles. The sparse and dense regions are highlighted to illustrate the transitions between primary, secondary and onset of dilation phases.

strain is computed based on the previous time step stress values, explicit integration schemes require limiting the time step size to avoid accumulating numerical errors. The solution obtained at a given time step is indeed not entirely satisfying the equation as the current viscoplastic strain rate is satisfying the previous time step stress values. To this end, we introduce a stress update algorithm adapted from the classical implicit integration scheme (elastic predictor–inelastic corrector method), which updates the stress tensor based on the strain increment at each time step. Our implementation is based on an iterative strategy for updating the viscoplastic strain until numerical convergence is achieved within a given time step. This iterative process comes with additional computational cost compared to an explicit integration scheme but lift the necessity to limit the time step size to avoid accumulating numerical errors. The advantage of an implicit integration scheme becomes predominant when dealing with large domains and problems at the cavern scale. The choice of time steps can only be driven by the choice of loading conditions and macroscopic response of the rock salt, whether than by the limiting explicit integration scheme.

6.2. Origins and controls on the onset of dilatancy

Our numerical results of cycling loading at the laboratory scale indicates that the rock salt samples can undergo dilatancy after a given time of cyclic loading. After this onset of dilatancy, the axial strain evolution deviates from its initial trend reaching higher strains than initially. Understanding what controls the onset of dilatancy is therefore essential to prevent possible salt cavern instability at the field case. Our results show that the timing of the onset of dilatancy does not depend on the cyclic loading frequency as all the cases considered (loading periods of 1, 2, 4 and 8 days) exhibit the onset of dilatancy at the 150 days timestamp. However, the amplitude of the axial cyclic loading influences the onset of dilatancy with higher stress values accelerating the time of dilatancy onset. The rock salt samples do not exhibit any signs of dilatancy for stress amplitudes below 12.5 MPa. It remains however unclear what processes control the onset of dilatancy. During classic creep and multi-creep tests, no onset of dilatancy was observed, whether experimentally nor numerically. It therefore implies that the cyclic nature of loading plays an essential role on the onset of dilatancy.

In our numerical experiments, the distribution of strain within the rock salt samples suggests that strain localization occurs concurrently to the onset of dilatancy. These two phenomena seemed to be intertwined, but it is still unclear whether one is the consequence of the other. Strain localization might cause a divergence in the macroscopic strain response of the rock salt sample. Such phenomena usually occurs when a mechanical stability occurs (Rudnicki and Rice, 1975). Future studies should investigate the relation between strain localization and onset of dilatancy.

6.3. Impacts for cyclic hydrogen storage

These results have important implication for the operation of underground hydrogen storage caverns. Maintaining structural stability requires minimizing viscoplastic deformation and delaying or preventing diffuse or profound dilatancy. Our results indicate that the magnitude of the cyclic stress magnitude is the primary parameter controlling the onset of dilatancy. In the context of hydrogen seasonal storage, it means that the hydrogen pressure amplitudes induced by injection and production rates could have a significant impact of the cavern wall stability. The duration of a storage cycle and of a production cycle could also play a significant role in the stability of the cavern wall, as the cyclic loading period impact the evolution of axial and volumetric strain after the onset of dilation. The operators should therefore monitor if possible the evolution of the cavern deformation to prevent or anticipate the onset of dilation by reducing the injection and production rates of hydrogen in the cavern. In the case of such an onset of dilation already occurred, the operators could increase the duration of the production and storage cycles to minimize the impacts of dilation on the cavern wall stability. In future studies, we will explore the impacts of realistic hydrogen injection and production schedules on the deformation of a rock salt cavern.

7. Conclusion

In summary, this study presents a comprehensive numerical implementation strategy for the RTL2020 viscoplastic constitutive model for rock salt using the open-source numerical simulator BEAVER, developed on the MOOSE framework.

The accuracy of the numerical formulation is demonstrated by validating key components of the model — specifically, the individual deviatoric strain-rate terms — against their corresponding analytical solutions. Furthermore, the full RTL2020 model is validated against experimental data from both short-term triaxial tests and long-term creep experiments using a single set of material parameters. Together, these results confirm the model's capability to reproduce the complex mechanical behaviour of rock salt across a broad range of loading conditions in a consistent and unified manner. Thus, underscoring the effectiveness of the proposed stress update algorithm in ensuring numerical accuracy and convergence of our RTL2020 implementation. More importantly, they highlight the reliability of the model in simulating the mechanical response of rock salt under complex stress paths and time-dependent loading conditions.

Application of the implemented model to numerical cyclic triaxial tests provides valuable insight into the potential behaviour of rock salt under conditions representative of hydrogen storage in underground salt caverns. Specifically, the simulation results show a clear sensitivity of rock salt deformation to the applied cyclic loading frequency and stress amplitude, which has implications for cavern stability and serviceability during hydrogen injection and withdrawal from salt caverns.

Future investigations will apply the implemented model to field-scale simulations of salt caverns and underground repositories, with particular emphasis on the thermo-mechanical effects relevant to subsurface hydrogen storage. Additionally, the RTL2020 model will be integrated into fully coupled multiphysics frameworks, such as Thermal-Hydraulic-Mechanical (THM) models, to enhance our understanding of rock salt behaviour in geo-energy storage systems. Furthermore, the current model does not incorporate fatigue damage associated with repeated cyclic loading. This limitation is particularly relevant for long-term hydrogen injection and withdrawal cycles, where fatigue processes may significantly influence cavern stability and failure risks. Therefore, future models should extend the RTL2020 model to account for fatigue damage and its evolution, enabling more realistic predictions of long-term cavern performance.

Overall, the implemented RTL2020 model provides high-quality numerical predictions and demonstrates strong potential as a valuable numerical constitutive model for simulating rock salt mechanical behaviour. Its open-source availability makes it readily accessible to the geomechanic scientific community and practitioners for simulating rock salt deformation, especially volumetric strain evolution and dilation processes relevant to geo-energy applications such as hydrogen storage.

CRediT authorship contribution statement

Ishmael D. Yevugah: Writing – original draft, Visualization, Software, Methodology, Investigation, Formal analysis. **Antoine B. Jacquey:** Writing – review & editing, Visualization, Validation, Supervision, Software, Methodology, Funding acquisition, Conceptualization.

Declaration of generative AI and AI-assisted technologies in the manuscript preparation process

During the preparation of this work the authors used GPT-5 in order to improve language and readability of the text. After using this tool/service, the authors reviewed and edited the content as needed and take full responsibility for the content of the published article.

Declaration of competing interest

The authors declare that they have no known competing financial interests or personal relationships that could have appeared to influence the work reported in this paper.

Acknowledgements

This work was supported by the Natural Sciences and Engineering Research Council of Canada (NSERC), under the Discovery Grants Program (grant number RGPIN-2024-04747). This research was enabled in part by support provided by Calcul Québec (calculquebec.ca) and the Digital Research Alliance of Canada (alliancecan.ca). The authors would like to thank Laura Blanco-Martín and Ahmed Rouhabi for sharing data of their laboratory experiments and for the discussions about this manuscript.

Appendix. Comparison of explicit and implicit update procedures

We compared the implicit update scheme for the RTL2020 model to an explicit implementation. The explicit implementation uses old values of stress (from the previous time step) for evaluating the viscoplastic strain rate as introduced in Eqs. (9), (10) and (12). The domain is a single-element cuboid subject to a classic short-term triaxial loading at constant confining pressure $\sigma_c = 5\,\text{MPa}$ and a constant axial strain rate of $\dot{\varepsilon}_a = 1.0 \times 10^{-5}\,\text{s}^{-1}$. Because the results are homogeneous in terms of stress and strain for this setting, a single element domain is sufficient to compare the two integration algorithms. We use the parameters summarized in Table 2 for the RTL2020 model. We used four different time step sizes and compare the results based on the choice of time-stepping. Time step size is a critical parameter for explicit integration algorithms which can affect their stability and accuracy.

Figs. A.10 and A.11 summarized the results of this comparison. Fig. A.10 shows the evolution of the differential stress as a function of the axial strain for the four time step sizes considered. Fig. A.11 shows the

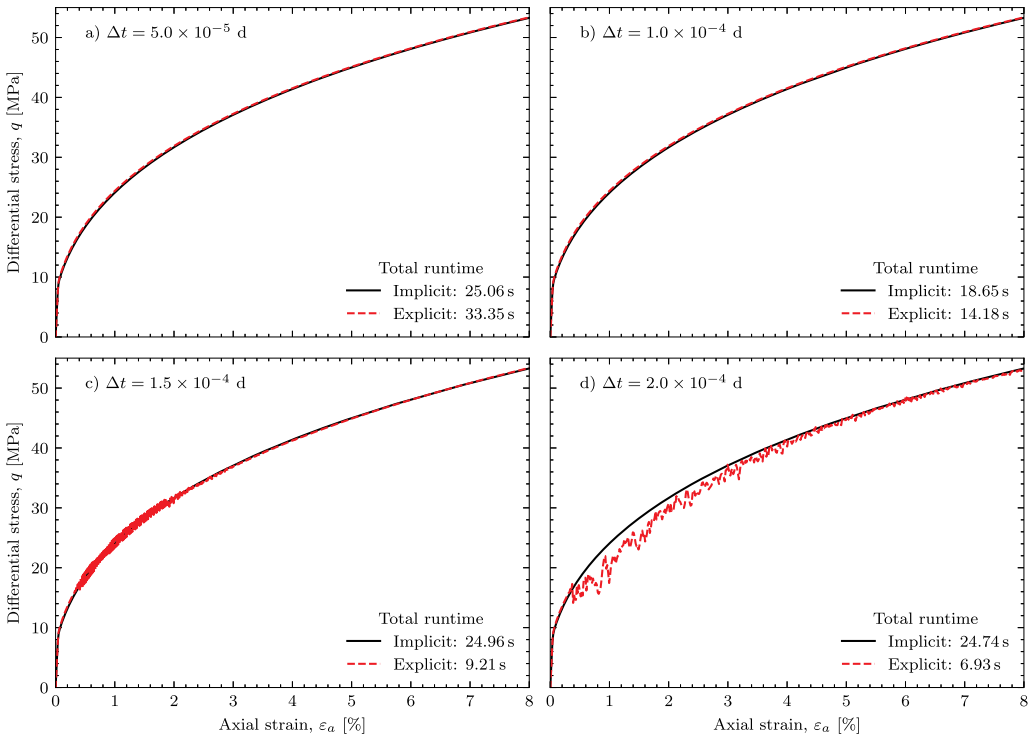


Fig. A.10. Evolution of the differential stress as a function of the axial strain for explicit and implicit integration algorithms of the RTL2020 model. Each panel corresponds to a time step size.

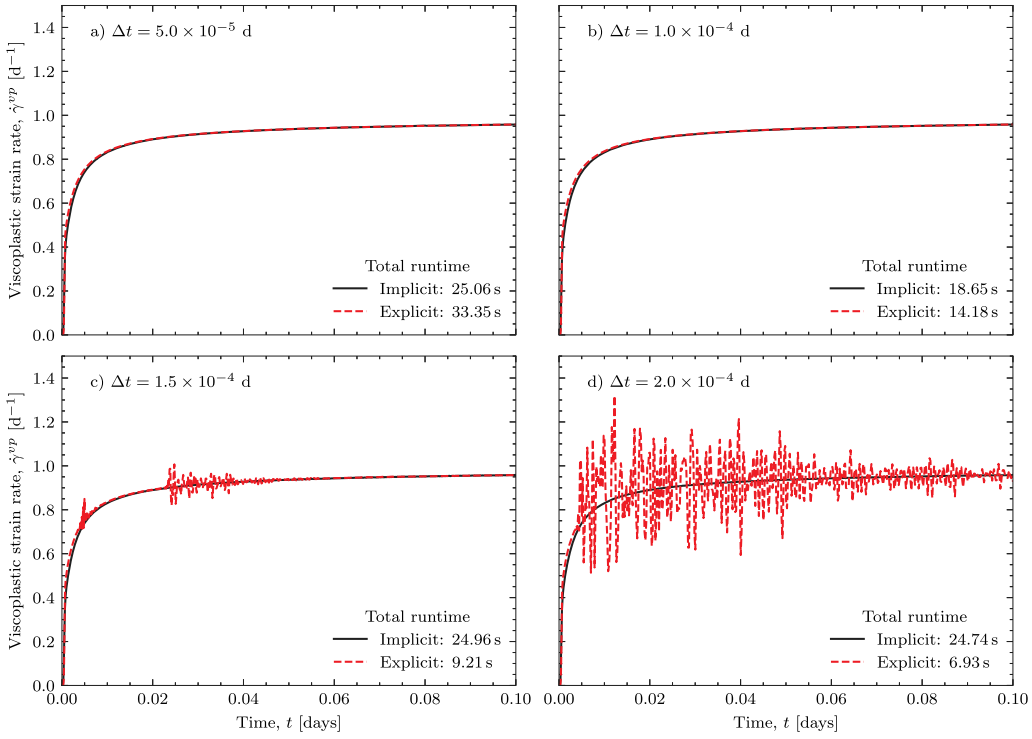


Fig. A.11. Evolution of the equivalent viscoplastic strain rate as a function of time for explicit and implicit integration algorithms of the RTL2020 model. Each panel corresponds to a time step size.

evolution of the equivalent viscoplastic strain rate as a function of time for the four time step sizes considered. For the two smaller time step sizes considered, both algorithms give almost exact responses in terms of stress and viscoplastic strain rate. However, for the two larger time step sizes, the explicit algorithm becomes unstable and gives oscillatory solutions in terms of viscoplastic strain rates which is also visible in the stress response. This illustrates one major limitation of explicit integration algorithms which can become unstable when the time step

size increases. On the other hand, the implicit integration algorithm gives similar responses for all four time step sizes, demonstrating its unconditional stability regarding time step size.

In terms of total runtime, the explicit algorithm is in general slightly faster (for the cases where it gives a stable response). For the smaller time step size, the explicit algorithm is significantly slower as it requires more non-linear iterations in the global solver. The implicit algorithm tends to require more run time when the time step size increases. This is usually due to the fact that for non-linear models, the implicit algorithm will require more internal iterations to converge. In conclusion, these observations show the unconditional stability of the implicit algorithm with respect to the time step size, even though it comes at higher computational cost when this time step size significantly increases.

Data availability

I have shared a reference to the data repository containing the code used in this manuscript.

References

Aubertin, M., Gill, D., Ladanyi, B., 1993. Modeling the transient inelastic flow of rocksalt. In: Proceedings of 7th Symposium on Salt, Kyoto, Tokyo. Vol. 1, pp. 93–104.

Azabou, M., Rouabhi, A., Blanco-Martín, L., Hadj-Hassen, F., Karimi-Jafari, M., Hévin, G., 2021. Rock salt behavior: From laboratory experiments to pertinent long-term predictions. Int. J. Rock Mech. Min. Sci. 142, 104588. http://dx.doi.org/10.1016/j.ijrmms.2020.104588.

Bagchi, C., Patwardhan, S.D., Iglauer, S., Ben Mahmud, H., Ali, M.F.J., 2025. A critical review on parameters affecting the feasibility of underground hydrogen storage. ACS Omega 10 (12), 11658–11696. http://dx.doi.org/10.1021/acsomega.4c10442.

Berest, P., Karimi-Jafari, M., Brouard, B., 2008. Comportement mécanique à très long terme des mines et cavernes dans le sel gemme: loi de Norton-Hoff ou loi de Lemaître? Rev. Française de Géotechnique (124), 45–59. http://dx.doi.org/10.1051/geotech/2008124045.

Blanco-Martín, L., Azabou, M., Rouabhi, A., Hadj-Hassen, F., 2023. Laboratory experiments on rock salt and phenomenological observations. Int. J. Rock Mech. Min. Sci. 170, 105452. http://dx.doi.org/10.1016/j.ijrmms.2023.105452.

Blanco-Martín, L., Rouabhi, A., Hadj-Hassen, F., Jaworowicz, J., Azabou, M., Hévin, G., Labaune, P., 2024. Creep of rock salt under a large range of deviatoric stresses. Rock Mech. Rock Eng. 1–14. http://dx.doi.org/10.1007/s00603-024-03841-6.

Boidy, E., Bouvard, A., Pellet, F., 2002. Back analysis of time-dependent behaviour of a test gallery in claystone. Tunn. Undergr. Space Technol. 17 (4), 415–424. http://dx.doi.org/10.1016/S0886-7798(02)00066-4.

Böttcher, N., Görke, U.-J., Kolditz, O., Nagel, T., 2017. Thermo-mechanical investigation of salt caverns for short-term hydrogen storage. Environ. Earth Sci. 76 (3), 98. http://dx.doi.org/10.1007/s12665-017-6414-2.

Carter, N.L., Hansen, F.D., 1983. Creep of rocksalt. Tectonophysics 92 (4), 275–333. http://dx.doi.org/10.1016/0040-1951(83)90200-7.

Chang, K.W., Ross, T.S., 2025. Cyclic loading–unloading impacts on geomechanical stability of multiple salt caverns for underground hydrogen storage. Int. J. Hydrog. Energy 102, 767–777. http://dx.doi.org/10.1016/j.ijhydene.2024.12.514.

Cristescu, N.D., Gioda, G., et al., 1994. Visco-Plastic Behaviour of Geomaterials. Springer, http://dx.doi.org/10.1007/978-3-7091-2710-0.

Cristescu, N., Hunsche, U., 1998. Time Effects in Rock Mechanics. Vol. 350, Wiley New York.

Dong, Z., Liu, B., Chen, T., Wang, Z., Li, H., Liu, Y., Li, Y., Shi, X., Zhao, W., 2025. Study on creep behavior of huai'an rock salt under triaxial cyclic loading with long periods. Rock Mech. Rock Eng. 1–18. http://dx.doi.org/10.1007/s00603-025-05225-w.

Dunne, F., Petrinic, N., 2005. Introduction to Computational Plasticity. Oxford University Press, http://dx.doi.org/10.1093/oso/9780198568261.001.0001.

Fan, J., Jiang, D., Liu, W., Wu, F., Chen, J., Daemen, J., 2019. Discontinuous fatigue of salt rock with low-stress intervals. Int. J. Rock Mech. Min. Sci. 115, 77–86. http://dx.doi.org/10.1016/j.ijrmms.2019.01.013.

Gholami, R., 2023. Hydrogen storage in geological porous media: Solubility, mineral trapping, H2S generation and salt precipitation. J. Energy Storage 59, 106576. http://dx.doi.org/10.1016/j.est.2023.106576.

Gunther, R.-M., Salzer, K., Popp, T., 2010. Advanced strain-hardening approach constitutive model for rock salt describing transient, stationary, and accelerated creep and dilatancy. In: ARMA US Rock Mechanics/Geomechanics Symposium. ARMA, pp. ARMA–10.

Günther, R.-M., Salzer, K., Popp, T., Lüdeling, C., 2015. Steady-state creep of rock salt: improved approaches for lab determination and modelling. Rock Mech. Rock Eng. 48 (6), 2603–2613. http://dx.doi.org/10.1007/s00603-015-0839-2.

Guo, Y., Yang, C., Mao, H., 2012. Mechanical properties of jintan mine rock salt under complex stress paths. Int. J. Rock Mech. Min. Sci. 56, 54–61. http://dx.doi.org/10.1016/j.ijrmms.2012.07.025.

Han, Y., Ma, H., Yang, C., Zhang, N., Daemen, J., 2020. A modified creep model for cyclic characterization of rock salt considering the effects of the mean stress, half-amplitude and cycle period. Rock Mech. Rock Eng. 53 (7), 3223–3236. http://dx.doi.org/10.1007/s00603-020-02105-3.

Harbour, L., Giudicelli, G., Lindsay, A.D., German, P., Hansel, J., Icenhour, C., Li, M., Miller, J.M., Stogner, R.H., Behne, P., Yankura, D., Prince, Z.M., DeChant, C., Schwen, D., Spencer, B.W., Tano, M., Choi, N., Wang, Y., Nezdyur, M., Miao, Y., Hu, T., Kumar, S., Matthews, C., Langley, B., Nobre, N., Blair, A., MacMackin, C., Rocha, H.B., Palmer, E., Carter, J., Meier, J., Slaughter, A.E., Andrš, D., Carlsen, R.W., Kong, F., Gaston, D.R., Permann, C.J., 2025. 4.0 MOOSE: Enabling massively parallel multiphysics simulation. SoftwareX 31, 102264. http://dx.doi.org/10.1016/j.softx.2025.102264.

Heusermann, S., Rolfs, O., Schmidt, U., 2003. Nonlinear finite-element analysis of solution mined storage caverns in rock salt using the LUBBY2 constitutive model. Comput. Struct. 81 (8–11), 629–638. http://dx.doi.org/10.1016/S0045-7949(02)00415-7.

Hou, Z., 2003. Mechanical and hydraulic behavior of rock salt in the excavation disturbed zone around underground facilities. Int. J. Rock Mech. Min. Sci. 40 (5), 725–738. http://dx.doi.org/10.1016/S1365-1609(03)00064-9.

Hughes, T.J.R., Taylor, R.L., 1978. Unconditionally stable algorithms for quasi-static elasto/visco-plastic finite element analysis. Comput. Struct. 8 (2), 169–173. http://dx.doi.org/10.1016/0045-7949(78)90019-6.

Hunsche, U.E., 1993. Failure behaviour of rock salt around underground cavities. In: Proceedings of the 7th Symposium on Salt. Vol. 1, pp. 59–65.

Jacquey, A.B., Regenauer-Lieb, K., Cacace, M., 2021. Thermomechanics for geological, civil engineering and geodynamic applications: numerical implementation and application to the bentheim sandstone. Rock Mech. Rock Eng. 54 (10), 5337–5354. http://dx.doi.org/10.1007/s00603-021-02503-1.

Jacquey, A.B., Yevugah, I.D., 2026. BEAVER: Multiphysics Geomechanics for Geoenergy applications. http://dx.doi.org/10.5683/SP4/KUUHZY.

Khaledi, K., Mahmoudi, E., Datcheva, M., Schanz, T., 2016. Stability and serviceability of underground energy storage caverns in rock salt subjected to mechanical cyclic loading. Int. J. Rock Mech. Min. Sci. 86, 115–131. http://dx.doi.org/10.1016/j.ijrmms.2016.04.010.

Labaune, P., Rouabhi, A., 2019. Dilatancy and tensile criteria for salt cavern design in the context of cyclic loading for energy storage. J. Nat. Gas Sci. Eng. 62, 314–329. http://dx.doi.org/10.1016/j.jngse.2019.01.009.

Labaune, P., Rouabhi, A., Tijani, M., Blanco-Martín, L., You, T., 2018. Dilatancy criteria for salt cavern design: a comparison between stress-and strain-based approaches. Rock Mech. Rock Eng. 51, 599–611. http://dx.doi.org/10.1007/s00603-017-1338-4.

Li, H., Ma, H., Zhao, K., Zhu, S., Yang, K., Zeng, Z., Zheng, Z., Yang, C., 2024. Parameter design of the compressed air energy storage salt cavern in highly impure rock salt formations. Energy 286, 129520. http://dx.doi.org/10.1016/j.energy.2023.129520.

Lindsay, A., Stogner, R., Gaston, D., Schwen, D., Matthews, C., Jiang, W., Aagesen, L.K., Carlsen, R., Kong, F., Slaughter, A., et al., 2021. Automatic differentiation in MetaPhysicL and its applications in MOOSE. Nucl. Technol. 1–18.

Liu, Y., Li, Y., Li, J., Xu, M., Shi, X., Ma, H., Dong, Z., Song, Z., Shangguan, S., 2025. Stability evaluation and key operational parameter design of ultra-deep salt cavern gas storage based on in-situ creep tests. Geoenergy Sci. Eng. 214111. http://dx.doi.org/10.1016/j.geoen.2025.214111.

Lüdeling, C., Naumann, D., Minkley, W., 2022. Investigation of fluid transport in rock salt under repository-relevant conditions – the PeTroS project. In: The Mechanical Behavior of Salt X. CRC Press, pp. 200–211. http://dx.doi.org/10.1201/9781003295808-19.

Minkley, W., Mühlbauer, J., Lüdeling, C., 2016. Dimensioning principles in potash and salt: stability and integrity. Rock Mech. Rock Eng. 49, 4537–4555. http://dx.doi.org/10.1007/s00603-016-1086-x.

Moghadam, S.N., Nazokkar, K., Chalaturnyk, R.J., Mirzabozorg, H., 2015. Parametric assessment of salt cavern performance using a creep model describing dilatancy and failure. Int. J. Rock Mech. Min. Sci. 79, 250–267. http://dx.doi.org/10.1016/j.ijrmms.2015.09.001.

Muhammed, N.S., Haq, M.B., Al Shehri, D.A., Al-Ahmed, A., Rahman, M.M., Zaman, E., Iglauer, S., 2023. Hydrogen storage in depleted gas reservoirs: A comprehensive review. Fuel 337, 127032. http://dx.doi.org/10.1016/j.fuel.2022.127032.

Munson, D.E., Dawson, P., 1979. Constitutive Model for the Low Temperature Creep of Salt (With Application to WIPP). Technical Report, Sandia Labs., http://dx.doi.org/10.2172/5729479.

Munson, D., Dawson, P., 1981. Salt-Constitutive Modeling Using Mechanism Maps. Technical Report, Sandia National Labs., Albuquerque, NM (USA); Cornell Univ., Ithaca, NY (USA).

Ramesh Kumar, K., Honorio, H., Chandra, D., Lesueur, M., Hajibeygi, H., 2023. Comprehensive review of geomechanics of underground hydrogen storage in depleted reservoirs and salt caverns. J. Energy Storage 73, 108912. http://dx.doi.org/10.1016/j.est.2023.108912.

Rouabhi, A., Labaune, P., Tijani, M., Gatelier, N., Hévin, G., 2019. Phenomenological behavior of rock salt: On the influence of laboratory conditions on the dilatancy onset. J. Rock Mech. Geotech. Eng. 11 (4), 723–738. http://dx.doi.org/10.1016/j.jrmge.2018.12.011.

Rudnicki, J.W., Rice, J.R., 1975. Conditions for the localization of deformation in pressure-sensitive dilatant materials. J. Mech. Phys. Solids 23 (6), 371–394. http://dx.doi.org/10.1016/0022-5096(75)90001-0.

Senseny, P., Hansen, F., Russell, J., Carter, N., Handin, J., 1992. Mechanical behaviour of rock salt: phenomenology and micromechanisms. In: International Journal of Rock Mechanics and Mining Sciences & Geomechanics Abstracts. Vol. 29, Elsevier, pp. 363–378. http://dx.doi.org/10.1016/0148-9062(92)90513-Y.

Shahmorad, Z., Salarirad, H., Molladavoudi, H., 2016. A study on the effect of utilizing different constitutive models in the stability analysis of an underground gas storage within a salt structure. J. Nat. Gas Sci. Eng. 33, 808–820. http://dx.doi.org/10.1016/j.jngse.2016.06.011.

Simo, J., Hughes, T., 1998. Numerical analysis of general return mapping algorithms. Comput. Inelasticity 219–239.

Sobolik, S.R., Ehgartner, B.L., 2011. Analyzing the Effect of Large Pressure Changes on the Stability of Large-Diameter Caverns for the Strategic Petroleum Reserve Using the Multi-Mechanism Deformation Model. Technical Report, Sandia National Lab.(SNL-NM), Albuquerque, NM (United States).

Tackie-Otoo, B.N., Haq, M.B., 2024. A comprehensive review on geo-storage of H2 in salt caverns: Prospect and research advances. Fuel 356, 129609. http://dx.doi.org/10.1016/j.fuel.2023.129609.

Tijani, M., 2008. Contribution À L'étude Thermomécanique Des Cavités Réalisées Par Lessivage Dans Des Formations Géologiques Salines (Ph.D. thesis). Université Pierre et Marie Curie-Paris VI, URL: https://theses.hal.science/tel-00430361.

Wang, L., Bérest, P., Brouard, B., 2015. Mechanical behavior of salt caverns: closed-form solutions vs numerical computations. Rock Mech. Rock Eng. 48, 2369–2382. http://dx.doi.org/10.1007/s00603-014-0699-1.

Wang, T., Yang, C., Ma, H., Li, Y., Shi, X., Li, J., Daemen, J., 2016. Safety evaluation of salt cavern gas storage close to an old cavern. Int. J. Rock Mech. Min. Sci. 83, 95–106. http://dx.doi.org/10.1016/j.ijrmms.2016.01.005.

Wang, J., Zhang, Q., Song, Z., Zhang, Y., 2021. Experimental study on creep properties of salt rock under long-period cyclic loading. Int. J. Fatigue 143, 106009. http://dx.doi.org/10.1016/j.ijfatigue.2020.106009.

Wolters, R., Lux, K., Düsterloh, U., et al., 2012. Evaluation of rock salt barriers with respect to tightness: influence of thermomechanical damage, fluid infiltration and sealing/healing. In: Proceedings of the Seventh International. Conference on the Mechanical Behavior of Salt (SaltMech7), Paris, 16-19 April 2012. pp. 425–434.

Yang, C., Wang, T., Qu, D., Ma, H., Li, Y., Shi, X., Daemen, J., 2016. Feasibility analysis of using horizontal caverns for underground gas storage: A case study of yunying salt district. J. Nat. Gas Sci. Eng. 36, 252–266. http://dx.doi.org/10.1016/j.jngse.2016.10.009.

Zhao, K., Ma, H., Zhou, J., Yin, H., Li, P., Zhao, A., Shi, X., Yang, C., 2022. Rock salt under cyclic loading with high-stress intervals. Rock Mech. Rock Eng. 55 (7), 4031–4049. http://dx.doi.org/10.1007/s00603-022-02848-1.